Lidar depolarization characterization using a reference system

Alkistis Papetta[1], Franco Marenco[1], Rodanthi-Elisavet Mamouri[2,3], Argyro Nisantzi[2,3], Ioana Elisabeta Popovici[4,5], Philippe Goloub[5], Maria Kezoudi[1], Stéphane Victori[4], and Jean Sciare[1]

[1]The Cyprus Institute, Nicosia, Cyprus
[2]Cyprus University of Technology, Limassol, Cyprus
[3]ERATOSTHENES Centre of Excellence, Limassol, Cyprus
[4]Cimel Electronique, Paris, France
[5]University of Lille, CNRS, LOA - Laboratoire d'Optique Atmosphérique, Lille, France

Correspondence: Alkistis Papetta (a.papetta@cyi.ac.cy)

Abstract. In this study, we will present a new approach for the determination of depolarization parameters of the Nicosia CIMEL CE376 lidar system, using the Polly^{XT} in Limassol as a reference instrument. The method is applied retrospectively to the valuable measurements obtained during the 2021 Cyprus Fall campaign. Lidar depolarization measurements represent valuable information for aerosol typing and for the quantification of some specific aerosol types such as dust and volcanic

5 ash. An accurate characterization is required for quality measurements and to remove instrumental artefacts. In this article, we use the Polly^{XT} reference calibrated depolarization lidar to evaluate our system's gain ratio and channel cross-talk. We use observations of transported dust from desert regions for this approach, with layers in the free troposphere. Above the boundary layer and the highest terrain elevation of the region, we can expect that for long transport aerosols local effects should not affect the aerosol mixture so that we can expect similar depolarization properties at the two stations (separated by ∼60 km). Algebraic

10 equations are used to derive depolarization parameters from the comparison of the volume depolarization ratio measured by the two systems. The applied methodology offers a promising opportunity to evaluate the depolarization parameters of a lidar system, in cases where a priori knowledge of the cross-talk parameters is not available.

1 Introduction

Understanding the aerosol vertical stratification can help in reducing the uncertainties related to aerosol radiative forcings which remain large (IPCC , 2021). For more accurate estimations it is essential to improve the knowledge of the aerosol

15 characteristics: shape, size and optical properties. The diversity of combinations of aerosol sources and transport mechanisms leads to the high variability of the distribution of aerosols with different characteristics, which makes their classification a complicated task (Di Iorio et al. , 2003).

Lidar has become a widely used tool for studying highly resolved information on the spatial and temporal distribution of

20 aerosols. On this, several key campaigns, such as SAMUM 1, 2 and the ASKOS experiment (Groß et al. 2011, Tesche et al. 2011, https://askos.space.noa.gr), were performed and successfully demonstrate the capabilities of lidar systems. These were not the first to demonstrate aerosol lidars, e.g. Reagan et al. 1977, Brogniez et al. 1992, Krueger 1993. In contrast to traditional set-ups with in situ or airborne sensors, like optical particle counters (OPC) or particle sizers (Di Girolamo et al. ,

2022; Kezoudi et al. , 2021), lidars (ground or satellite-based) can provide information on the vertical structure up to the upper
25   troposphere and temporal variability. In addition, it provides insights on aerosol size and optical properties.

The contribution of lidar to greater science is undoubtedly important as it is a fundamental tool for monitoring anthropogenic and natural aerosols. Sand and dust storms, or volcanic ash transport in case of volcanic eruptions, can impact human health and everyday life. WMO Sand and Dust Storm Warning Advisory and Assessment System (SDS-WAS), benefits from available lidar networks (e.g. EARLINET, Bösenberg (2003)) for the monitoring of vertical profiles of winds and aerosols (Basart et
30   al. , 2019). Similarly, lidars installed across different locations aim to improve detection and aid forecasting of volcanic ash in the event of future eruptions, by providing observations to local Volcanic Ash Advisory Centres (VAAC) (Sassen et al. , 2007; Osborne et al. , 2022a).

The addition of a depolarization channel on a lidar system offers the capability to discriminate between different types of aerosols based on the depolarization ratios, for example, low depolarizing urban aerosols and high depolarizing dust aerosols,
35   or liquid and ice clouds. Discriminating between liquid and ice water can provide a better understanding of the aerosol-cloud interactions. Aerosols can change the properties of clouds and therefore affecting indirectly their radiative forcing (Senior and Mitchell , 1993; Fowler and Randall , 2002). Aerosol typing can be quite complex when the observed atmospheric layers consist of multiple aerosol types.

Lidar depolarization measurements represent an excellent method to detect and quantify some specific aerosol types such
40   as dust and volcanic ash (Cairo et al. , 1999; Tesche et al. , 2009; Freudenthaler et al. , 2009). Using this information, several studies aim to describe the properties and temporal evolution of each of the aerosol layers types (Hoffmann et al. , 2010; Ansmann et al. , 2011; Marenco and Hogan , 2011). They also permit to the distinction between ice crystals and water droplets (Ansmann et al. , 2005) and to discriminate the type of polar stratospheric clouds (Toon et al. , 2000). This technique is simple and reliable and is not as limited by daylight background as in the case of acquiring Raman signals.

45   Spherical particles in the atmosphere have no depolarization for 180° backscattering (Van de Hulst , 1957), hence a depolarization signal is an indication of non sphericity such as in ice crystals or irregular aerosols. Most lidar systems use linearly polarised lasers (linear depolarization measurements), and such systems are used also in this paper. Some circular polarisation lidar systems exist, such as eVe, which provide useful information for layers with oriented particles and where multiple scattering cannot be neglected (Paschou et al. , 2022).

50   Volume depolarization ratio (VDR) is defined as the ratio between the atmospheric cross sections for cross-polarised and co-polarised backscattering, and is a measure of the overall properties of the atmospheric volume, comprising a mixture of molecules and particles. This is typically measured by means of a polarising beamsplitter in the receiving system, and taking the ratio of signals in the two channels. In reality, the measurement is more complex than this, and it requires to account for the gain ratio of the channels and for the cross-talk between them: this is what here we refer to as the determination of the lidar
55   depolarization parameters. If this step is not achieved correctly, systematic errors appear with a significant impact.

Well characterized VDR measurements permit on the one hand reconstruction of the total lidar signal, by the recombination of the two channels: this is needed for the retrieval of the particle backscattering and extinction coefficients. On the other hand, they permit the computation of the particle depolarization ratio (PDR), which abstracts from the influence of air molecules and

is hence an intrinsic property of the particles (Freudenthaler et al. , 2009). In a well characterised lidar system for depolarisation, the channel gain ratio must be well known, as well as all the elements contributing to an imperfect separation of the depolarisation channels in the hardware. The latter include the polarising beam splitter transmittances and reflectances for the co-polar and cross-polar beams, as well as the laser polarisation purity and its rotation angle compared to the frame of reference of the receiver (Freudenthaler et al. , 2009). In particular, the laser rotation angle ϕ is not easily known, and an additional experimental apparatus has been used in a few papers in order to quantify it (Alvarez et al. , 2006; Belegante et al. , 2018; Osborne et al. , 2022b). The additional apparatus consists of a rotatable half way plate added in front of the receiver optical path, and a calibration sequence has to be performed where atmospheric measurements are acquired by artificially varying the system's cross-talk through the rotation of the half-wave plate.

At the Cyprus Institute, we have recently acquired a new compact CIMEL CE376 lidar system, which we have operated continuously in Nicosia, Cyprus, since September 2021. This is a low power and very compact 2 wavelength lidar system, ideal for campaigns and mobile observations, able to operate in all weather conditions, and able to detect the molecular signal up to 10 km in the daytime and 18 km in the nighttime with a good signal-to-noise ratio. We have however found an issue in the initial depolarization calibration, related to the observed VDR of purely molecular layers which is too high compared to the theoretically expected value (Behrendt and Nakamura , 2002). Whereas a technological solution is planned with CIMEL in the near future, this paper is about a method for correcting past data, by correlating the lidar measurements to a reference calibrated lidar system, that is also located on the island. This will be called the atmospheric characterization approach to the lidar depolarization parameters.

In Section 2, we present the depolarization lidar equations to be used for the depolarization characterization. Following Sections 3 and 4, we provide a description of the systems used in this study, focusing on the technical characteristics and locations. Section 5, presents the lidar depolarization characterization methodology providing demonstration examples from past observations. Finally, Section 6, summarizes and concludes the main findings of the application of the discussed method.

2 Theoretical concept

In an ideal depolarization lidar, the range corrected signal in the co-polar and cross-polar channels, $P^{\|}$ and $P^{\perp}$, can be expressed as follows, in the function of the atmospheric volume cross sections $\beta^{\|}$ and $\beta^{\perp}$ for non depolarising and depolarising backscattering, respectively:

$$P^{\|}(R) = K^{\|}\, T(R)\, \beta^{\|}(R) \tag{1}$$

$$P^{\perp}(R) = K^{\perp}\, T(R)\, \beta^{\perp}(R), \tag{2}$$

where R is the range, $T(R)$ is the two way atmospheric transmittance between ranges 0 and R, and $K^{\|}$, $K^{\perp}$ are the lidar constants for both channels.

The VDR is the ratio between $\beta^{\perp}$ and $\beta^{||}$, and in the ideal case it is computed as:

$$D = \frac{\delta^*}{K^*}, \tag{3}$$

where $\delta^* = P^{\perp}/P^{||}$ is the ratio of the two lidar signals (a sort of uncalibrated depolarization ratio), and $K^* = K^{\perp}/K^{||}$ is the gain ratio between the two channels. For an ideal lidar, determining K^* is all that is needed to calibrate depolarization. Once this is done, then the total lidar range corrected signal, P, can be reconstructed as a signal proportional to $\beta^{||} + \beta^{\perp}$. Hence:

$$P = P^{||} + \frac{P^{\perp}}{K^*}. \tag{4}$$

$P(R)$ is what will be used in aerosol inversion schemes such as Fernald-Klett (Klett , 1985; Fernald , 1984) or Raman inversion (Ferrare et al. , 1998).

For a real depolarization lidar system, the equations need to account for the cross-talk between the two channels, through the cross-talk constants γ and ϵ, expressing respectively how much co-polar signal enters the cross-polar channel and vice versa.

$$P^{||} = K^{||}\, T\, (\beta^{||} + \epsilon\, \beta^{\perp}) \tag{5}$$

$$P^{\perp} = K^{\perp}\, T\, (\beta^{\perp} + \gamma\, \beta^{||}) \tag{6}$$

$$D = \frac{\delta^* - K^*\, \gamma}{K^* - \epsilon\, \delta^*} \tag{7}$$

$$P = (1 - \gamma)\, P^{||} + (1 - \epsilon)\, \frac{P^{\perp}}{K^*} \tag{8}$$

These full equations are going to be applied for the determination of depolarization parameters. In Freudenthaler et al (2009), the approach is to assume that we know our system well enough to know the value of γ and ϵ, so that calibration only involves determining K^*. In our case, we assume we don't know our system to this point, and we will retrieve these parameters from observations and from a reference system (we call this the three-parameter depolarization characterization, since K^*, γ and ϵ are to be retrieved).

The effect of γ will usually dominate in low depolarization layers (e.g. particle free layers), so that we can attempt at simplifying Eq. 7 by neglecting ϵ:

$$D = \frac{\delta^*}{K^*} - \gamma, \tag{9}$$

which can be summarised in a phrase by saying that, in addition to knowing the gain ratio K^*, we must also know the "depolarization of the lidar system", γ, or alternatively that depolarization equation involves a multiplicative and an additive parameter. Whereas it may not be the most correct way to neglect ϵ for all lidar systems, this simplified equation seems to work for some systems: for example, it was used in Marenco and Hogan (2011), Eq. (5) and in Chazette et al (2012), Eq. (6). We call the approach using this simplified equation the two-parameter depolarization characterization (given that only K^* and γ can be determined).

The following sections investigate these approaches and will highlight their advantages and drawbacks, and compare their outcomes.

3 Instruments

3.1 CIMEL Lidar system

As it was briefly introduced before, CIMEL CE376 is a compact elastic backscatter lidar developed by CIMEL in France (seen in Figure 1). It is a dual wavelength polarization lidar equipped with a laser diode and a frequency doubled Nd:YAG laser, operating in the near infrared (808 nm) and green (532 nm) with a repetition rate of 4.7 kHz. It has a small FOV for emission (50 μrad) and reception (120 μrad) making it suitable for aerosol profiling. It measures backscatter signals in three reception channels, one for the infrared and two for green, co-polar and cross-polar channels. The lidar uses photon counting acquisition through avalanche photodiode detectors (SPCM-AQRH modules from Excelitas), for all the reception channels (schematic in Appendix D). The system has day and night operation with a typical detection altitude of around 10 km for the day and 18 km for the night. The signal is recorded in 2048 successive bins spaced by 15 m in the vertical direction from 100 m up to a range of 30 km. The integration time is 1s. Before the raw CIMEL lidar data can be used for the depolarization characterization method, it must be pre processed to correct detection errors and remove ambient background signals on all three channels. The basic pre processing includes dead time, dark count, quantum efficiency and background correction of the raw CIMEL data. Furthermore, data are filtered for quality assurance based on housekeeping parameters. Further post processing of the CE376 data is described in Section 4.

The CIMEL lidar was installed in September 2021 at the Cyprus Institute premises in Nicosia, Cyprus [N35°8′29.23″, E33°22′51.49″] and has been running continuously since.

Nicosia is located in the center of the island, between the largest mountain ranges of Cyprus: Troodos stretching across a third of the island peaking at 1952 m and Kyrenia mountain range that runs along the northern coast of the island peaking at 1024 m (see Figure 3). The aerosol mixture above Nicosia is often a mixture between dust particles and anthropogenic haze.

The depolarization calibration suggested by the manufacturer follows the $\pm45°$ method described by Freudenthaler (Freudenthaler et al. , 2009). To rotate the plane of polarization a half-wave plate (HWP) is used in front of the polarizing beamsplitter

Figure 1. CE376 lidar with thermal enclosure on CYI premises roof in Nicosia (left) and Polly^{XT} container housing in CUT premises in Limassol (tight).

cube. The $0°$ position of the HWP is found by maximizing the signal on the co-polar channel and minimizing the cross-polar. Note that a priori knowledge of the cross-talk parameters is required for this method, therefore we use transmittances (Tp, Ts) provided by the polarizing beam splitter (PBS) manufacturer (shown in Table 1) for the calibration constant (V*) calculations.

	Tp (%)	Ts (%)	V*
Period 1 (21/09/2021-05/01/2022)	1.03	99.92	1.17
Period 2 (11/01/2022-now)	0.45	99.8	0.78

Table 1. Characteristic $\pm 45°$ PBS calibration coefficient (V*) and transmittances for the parallel and perpedicular polarizations (T_p and T_s).

145 A depolarization calibration was performed during the installation of the lidar in order to derive the calibration coefficient V^*, for the depolarization channel at 532 nm (found to be $V^* = 1.17$. $V^* \simeq K^*$, see Appendix A to understand the exact relationship between V^* and K^*). However, the molecular depolarization at 5-5.5 km was measured to be ~ 40 times larger than the theoretical molecular depolarization for the lidar characteristics (3.6E-3 for a narrow filter of 0.2 nm, according to Behrendt and Nakamura , 2002). As this issue seemed to originate from the instrument and not the calibration, on January 150 2022 CIMEL intervened on site on the instrument to replace the PBS with a new one and repeated the calibration (giving a new $V^* = 0.78$). The PBS replacement did not suffice to improve the polarization measurements issue, which could be due to optical components inside the receiver and/or residual polarisation from the laser. Figure 2, summarizes these findings by comparing the theoretical molecular VDR (D_m) to two profiles on aerosol free days from periods 1 and 2.

There are technical solutions that can be followed in order to improve the characterization of the system. Adding a mo-
155   torized half-wave plate can reduce the human induced uncertainty during the calibration procedure, but this wouldn't resolve
the cross-talk issue. Moreover, wire grid polarizers can be added on the PBS to reduce the cross-talk. The latter is planned
for the near future, but wouldn't help to correct the depolarization measurements that were acquired so far. Such valuable
measurements were obtained for more than 1 year in Nicosia, including the Fall campaign that was performed in Cyprus in
2021. This research campaign was performed by Cyprus Atmospheric Observatory (CAO: https://cao.cyi.ac.cy/) and the Un-
160   manned Research Laboratory (USRL, Kezoudi et al. , 2021) of the Cyprus Institute (CYI), in collaboration with the Cyprus
Atmospheric Remote sensing Observatory (CARO) of the ERATOSTHENES Centre of Excellence (ECoE) with the aim of
characterizing dust properties above the island (Kezoudi et al., Fall campaign paper, manuscript in preparation). During this
campaign, measurements were obtained by remote sensing (lidars, ceilometers and sunphotometers) and UAV based instru-
mentation (optical particle counters, backscatter sondes, and impactors able to collect dust samples). It is essential to have a
165   method to characterize the depolarization for past data in order to make use of the CIMEL lidar in synergy with the rest of the
instrumentation, hence the motivation for this paper.
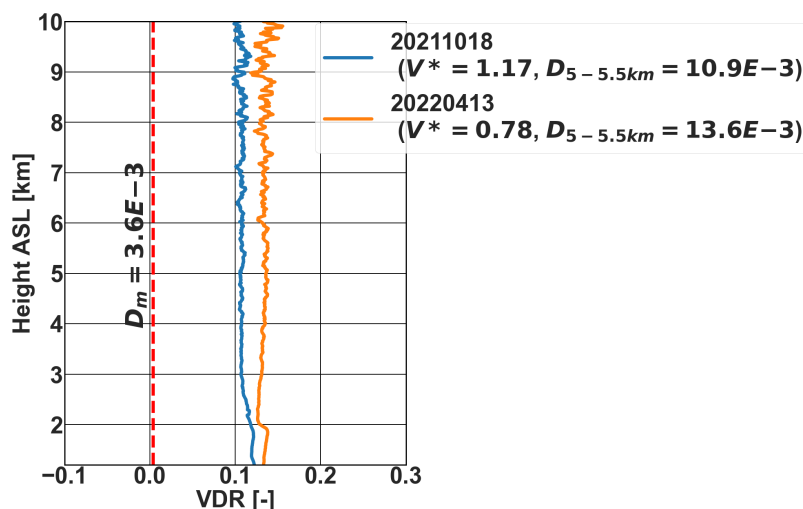
Figure 2. Measured volume depolarization with CIMEL following $\pm 45°$ calibration for two cases dominated by molecular scattering above
3 km. Blue for the case from period 1 and orange for period 2. The red dashed line shows the theoretical molecular depolarization ratio

3.2   Polly^{XT} system

Polly^{XT} is a well characterized instrument, which follows specific calibration and data quality assurance procedures according
170   to EARLINET, hence it serves as the reference system in this paper. It was set up in October 2020 for continuous operation,
at Limassol, Cyprus [N34°40′36.01″, E33°2′39.01″] (location seen on Figure 3). Polly^{XT} is a transportable aerosol multi-
wavelength Raman and polarization lidar that enables the determination of the particle backscatter coefficients at 355, 532, and

1064 nm and extinction coefficients at 355 and 532 nm. In addition, two depolarization channels at 532 and 355 nm are set up to determine the shape of the aerosol particles from measurements of the (particle) linear depolarization ratio. (Engelmann et al. , 2016; Althausen et al. , 2009).

Limassol is located on the other side of the Troodos mountain range with respect to Nicosia. Due to the topography, complex aerosol mixtures are observed over Limassol consisting of desert dust arriving from the Sahara or Arabian desert, marine particles and urban pollution.

In this paper, the systematic errors related to the volume linear depolarization ratio of the Polly^{XT} are taken from the study done by Bravo-Aranda et al. (2016), where the author provides some indications of the systematic errors based on the lidar model of Freudenthaler et al. (2016). Based on that model $\Delta D(0.45) = 0.0156$ for dust layers and $\Delta D(0.004) = 0.0057$ for molecular range. The considered Polly^{XT} profiles of this paper are presented together with the aforementioned systematic error and statistical uncertainty calculated of the 1 hour averaged profiles.
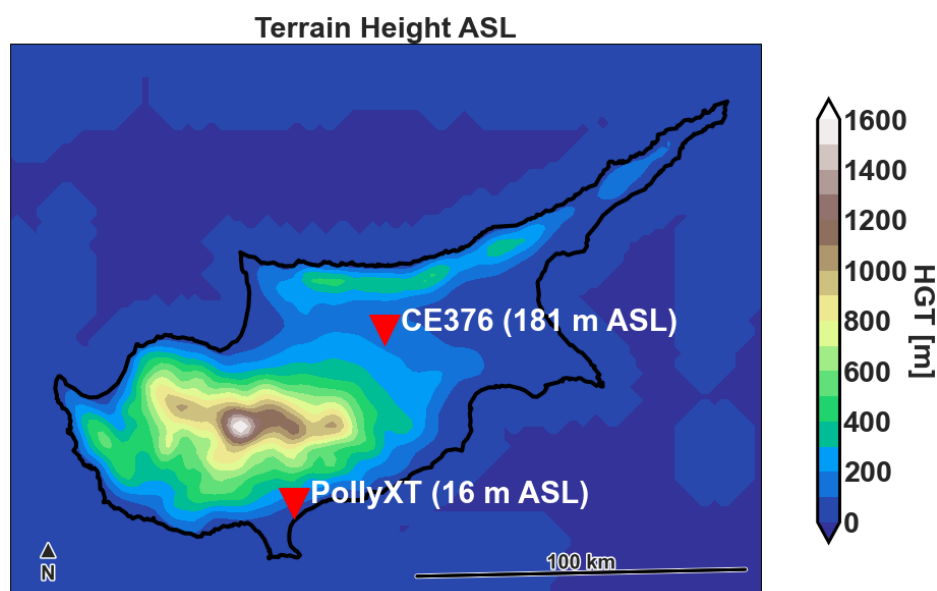
Figure 3. Cyprus topographic map. The red pins indicate the locations of CIMEL CE376 in Nicosia and Polly^{XT} in Limassol.

4 Lidar depolarization characterization

In this section, we describe the methodology on how to determine depolarization parameters for the CIMEL lidar using the Polly^{XT} reference system for selected cases during dust events, for both periods 1 and 2. For the so called atmospheric depolarization characterization, we selected cases with dust layers that were part of the long distance advection of dust from the nearby deserts. Dust over the island is considered to be fairly homogeneous in the free troposphere and the distance between the Polly^{XT} and CIMEL lidar is much smaller than the distance travelled from source regions. Ideally, an intercomparison

190 should be done with both systems side by side to sample the same air mass. If this is not possible, for example when already existing data need to be corrected, someone has to select the cases carefully. For this paper, data were already available from the Cyprus Fall Campaign 2021, during which the two stations are separated by ~ 60 km. Due to this spatial distance between the two lidars and the mountains in the area, the VDR could change because of atmospheric changes e.g. temperature and relative humidity.

195 Hence, it is important to carefully select the cases for which both lidars measure similar VDR profiles based on the following criteria: (i) dates with dust layers detected above 3 km, to exceed the topographic obstacle of Troodos in the centre of the island, (ii) molecular signal above the dust layer, (iii) only nighttime profiles are selected to improve SNR, (iv) cloud free scenes or high level clouds only and (v) general assessment of the meteorology to confirm the origin of air masses as being due to long range transport. For all the cases used for the determination of depolarization parameters, we have performed HYSPLIT back

200 trajectories (Figure 4) to demonstrate that the air masses are produced in long distance and therefore are not affected by local effects.

The method is based on some important assumptions. Firstly, we assume that the dust volume depolarization is identical above 3 km in the measured profiles by the two systems. The second assumption is that there is no time shift between the two measurements. Only depolarization at 532 nm will be considered from the Polly^{XT} which is the wavelength of the CIMEL

205 lidar depolarization measurements that we wish to characterize.

Before comparing the profiles from the two instruments we apply time integration and smoothing on the CE376 measurements to a common temporal and vertical range resolution (1 hour and 82.5 m respectively). As the last step, we should correct for the vertical shift observed on the profiles of the two lidars. This correction aims to remove the altitude difference between the two locations in the case of a sloping layer (more on the correction in Appendix B).

210 We demonstrate the proposed depolarization characterization approach using profiles from two nights that follow the criteria described before. As the dataset was limited (due to the selection criteria i.e. dust layer above 3 km), the selected cases are taken from days with uniform dust layers over the island and for which the profiles of the two systems do not seem to be influenced by any local phenomena. The first timestamp 26 November 2021 22:00 is taken from a 5 day long dust event arriving from the Saharan desert (confirmed with HYSPLIT back trajectories), resulting in a daily average AOD$_{500nm}$ value of 0.14 and

215 0.08 over Nicosia and Limassol respectively (AERONET, https://aeronet.gsfc.nasa.gov). During this event, one uniform dust layer was extending from 2 up to 4 km. The second timestamp on 16 February 2022 at 21:00 is extracted from a relatively shorter event (2 day long) during which dust was advected also from the Saharan desert to Cyprus, but this time not as uniform in the vertical direction with some distinct layers seen around 4 km. A cirrus cloud layer was also identified from 6 to 10 km. For the second event, the daily AOD$_{500nm}$ average over Nicosia was 0.20, whilst no data were available from Limassol's

220 sunphotometer. The VDR of the days from which we extracted the timestamps are seen in Figure 5.

4.1 Two-parameter depolarization characterization

In order to find the gain ratio K^* and cross-talk γ we create a system of equations following Eq. 9 using the reference measurements of the average depolarization D_d^{ref} of a dust layer and the theoretical molecular VDR, $D_m = 3.6E\text{-}3$ for the
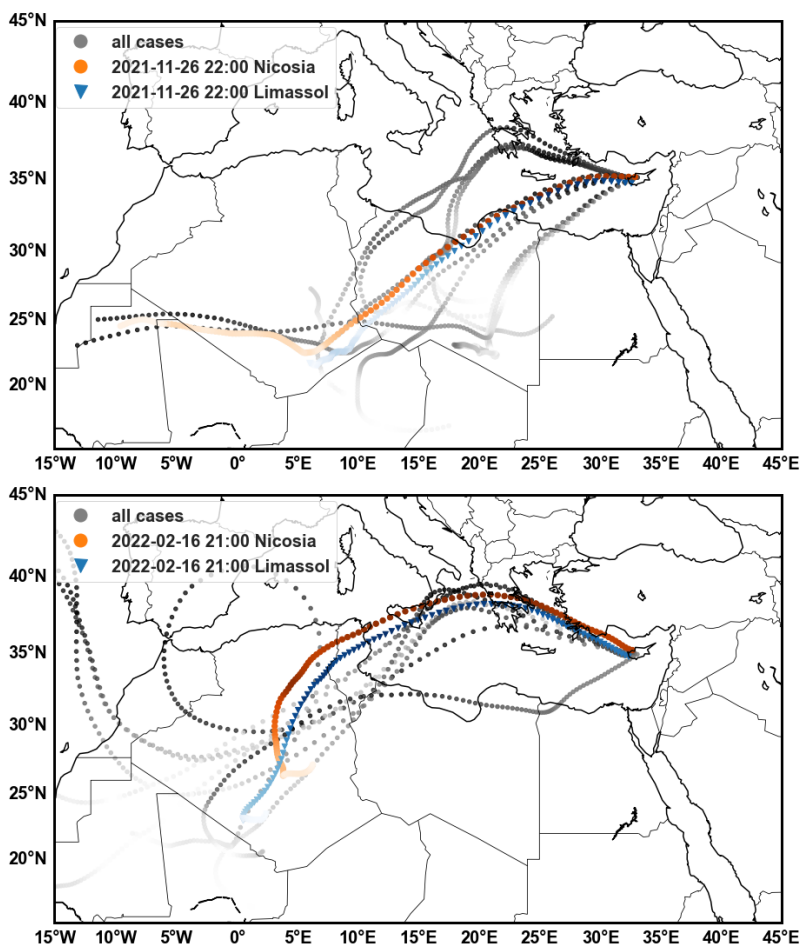
Figure 4. HYSPLIT back trajectories (https://www.ready.noaa.gov/) ending in Nicosia for all the selected cases for the first (top) and second period (bottom)(the two periods are separated for illustration purposes). The two demonstration cases are highlighted for endpoints in Nicosia (orange) and Limassol (blue). Color scaling indicates the elevation of the layer with light being at ground level and darker increasing altitude.

CIMEL lidar as mentioned also in Section 3.1. For every examined profile, we select D_d^{ref} from the reference instrument and
225 the channel signal ratio of dust (δ_d^*) and of the molecular layer (δ_m^*) from the CIMEL instrument by averaging the values in the corresponding ranges. The resulting equations are:

$$D_{ref}^d = \frac{\delta_d^*}{K^*} - \gamma, \tag{10}$$

$$D_m = \frac{\delta_m^*}{K^*} - \gamma. \tag{11}$$
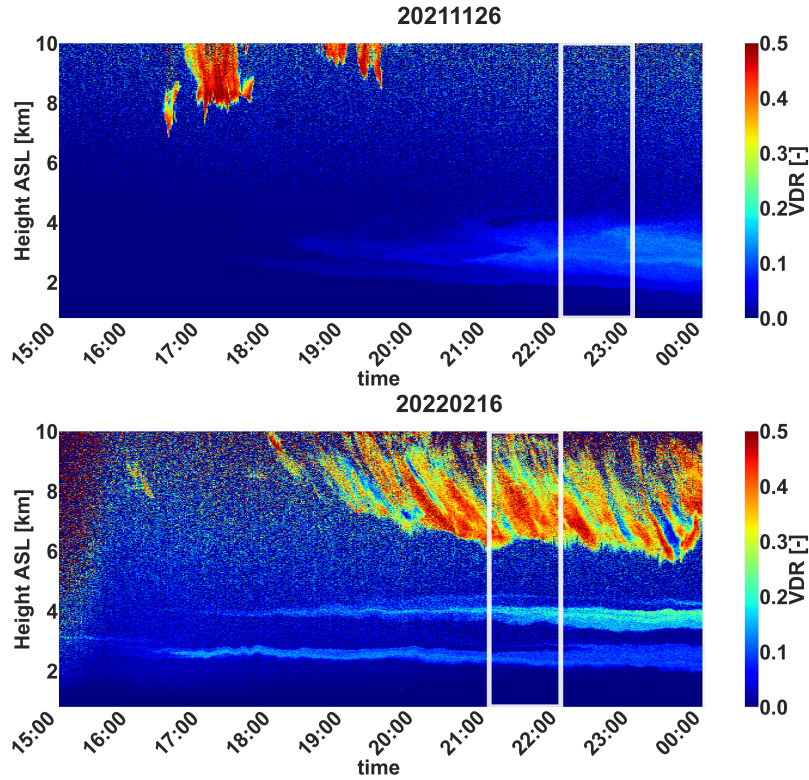
Figure 5. Corrected VDR from the CIMEL lidar using the two-parameter approach for 26 November 2021 (top) and 16 February 2022 (bottom) in 1 minute time resolution. White lines indicate the 1 hour average intervals of the demonstrated cases.

With two unknowns and two equations, we can solve for K^* and γ:

$$K^* = \frac{\delta_d^* - \delta_m^*}{D_{ref}^d - D_m} \tag{12}$$

$$\gamma = \frac{\delta_m^* D_{ref}^d - \delta_d^* D_m}{\delta_d^* - \delta_m^*} \tag{13}$$

Figure 6 shows the application of the method described above for the cases considered in the first and second periods. In these figures, the resulting VDR profile (D_2) is compared to the reference Polly^{XT} VDR profile (D_{ref}) and the CIMEL VDR profile (D_1) calculated based on the $\pm45°$ method described in Section 3.1. For the first case (26 November 2021 22:00) D_{ref}^d and δ_d^* are selected in the range 3.4-3.6 km. The molecular range δ_m^* for this case is chosen between 6-6.5 km. The VDR value at this molecular range after the correction is 3.5E-3 whilst the relative difference at the dust layer is reduced from 0.2 to 0 for $D_2 - D_{ref}$ compared to $D_1 - D_{ref}$. For the second case (16 February 2022 21:00) D_{ref}^d and δ_d^* are selected in the range 4-4.2

km, whilst molecular range δ_m^* is found to be between 5-5.5 km. In this range, the D_m is 2.6E-3, not far from the theoretical.

240 At the reference dust layer, the relative difference $D_2 - D_{ref}$ after the two-parameter method is in the order of 0.01. In general, for the second period, the D_1 improved at the high depolarizing layers but not at the molecular. The determined depolarization parameters correct the depolarization values (D_2) both at high and low depolarizing layers, which is confirmed by the presented cases where molecular VDR approaches the theoretical with only small deviations.
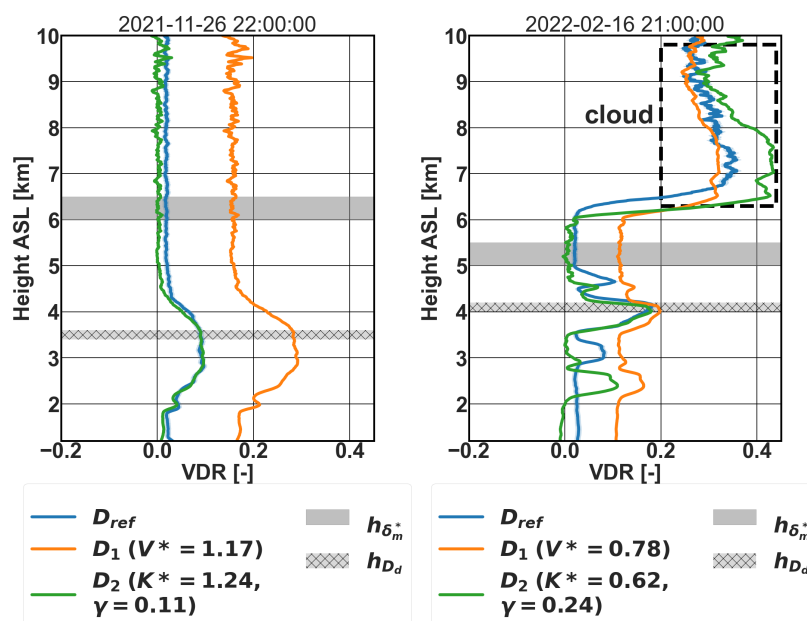
Figure 6. VDR corrected profiles for 26 November 2021 22:00 (left) and 16 February 2022 21:00 (right) using the two-parameter approach. Corrected profiles (D_2) are compared to the reference Polly^{XT} lidar profile (D_{ref}) and the CIMEL lidar profile using the $\pm 45°$ calibration factors (D_1). The shaded regions indicate the reference ranges used for dust and the molecular layers. Left a case from period 1 and on the right case from period 2. Systematic errors of the reference instrument are shown with a blue shade.

The depolarization parameters K^* and γ are calculated for a number of profiles from the first and second periods. The

245 variation of the derived parameters for the two different periods vs time is seen in Figure 7. The parameters vary little over time for the selected periods and so are the statistical properties such as average and variance. We choose to use the average of the parameters to correct the depolarization on different dates, hereinafter referred to as average depolarization parameters ($\langle K^*\rangle, \langle\gamma\rangle$). The average depolarization parameters are summarized in Table 2. It is observed from the Table that the values of V* calculated by the $\pm 45°$ calibration are close to the estimated K^* calculated by the authors using the atmospheric

250 depolarization characterization approach. This work however adds an estimate of γ, which was otherwise not available.

Figures 8 show the VDR profiles using the average depolarization parameters given in Table 2 for the two individual cases shown previously in Figure 6. There is no important effect on the profiles from the application of the average parameters, with

	Period 1			Period 2		
$\pm 45°$ **calibration**	V* = 1.17			V* = 0.78		
two-parameter	K* = 1.150 ± 0.068	γ = 0.1186 ± 0.0076		K* = 0.692 ± 0.048	γ = 0.214 ± 0.023	
three-parameter	K* = 1.10 ± 0.13	γ = 0.123 ± 0.027	ε = -0.36 ± 0.41	K* = 0.680 ± 0.074	γ = 0.24 ± 0.04	ε = -0.01 ± 0.20

Table 2. Average depolarization parameters for each examined period given with the standard deviation. All values are rounded to two significant figures for the standard deviation.
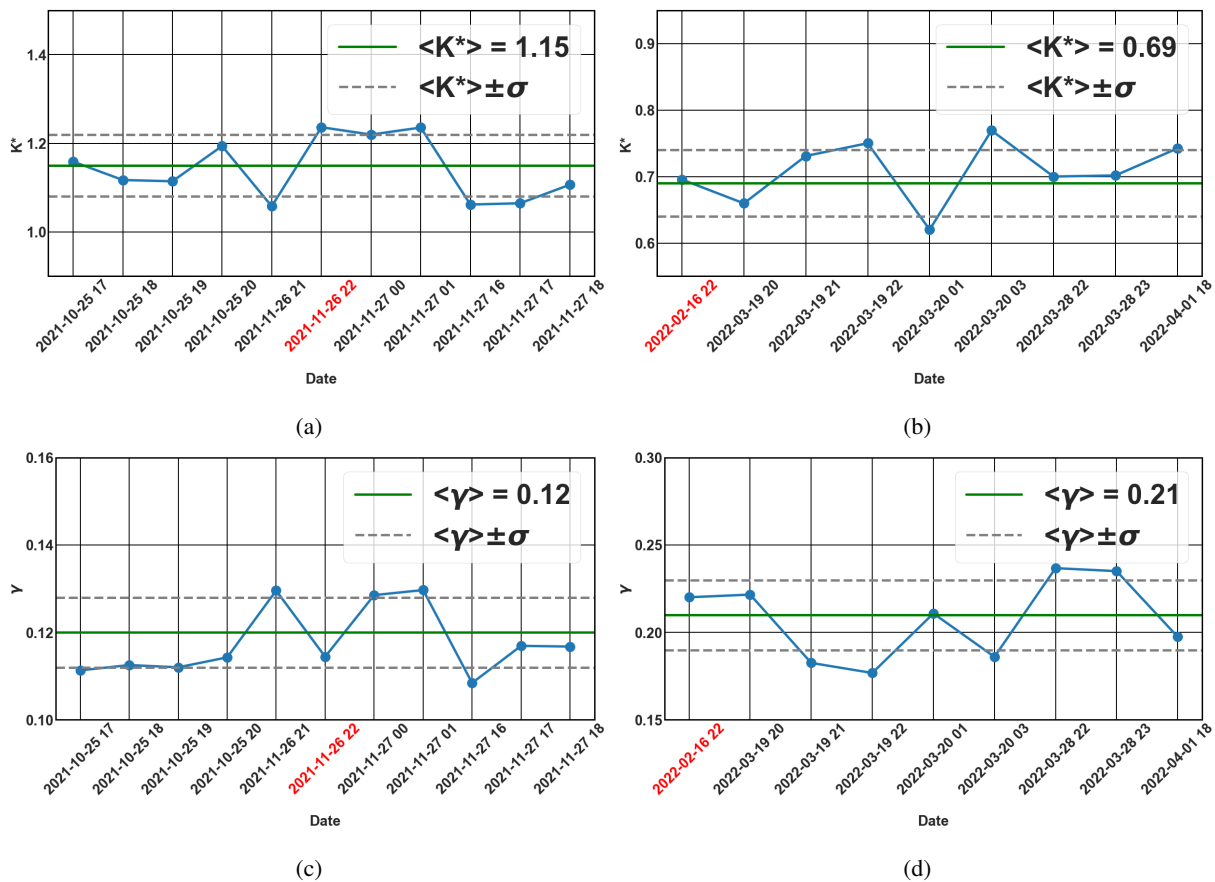
Figure 7. two-parameter approach derived depolarization parameters vs time for the first period (a,c) and second period (b,d). The timestamps of the cases shown in Figure 6 are highlighted in red colour.

low and high depolarizing layers being represented well. Any observed variations remain within the uncertainty of the method. The uncertainty shown in Figure 8 was propagated as described in Appendix C.
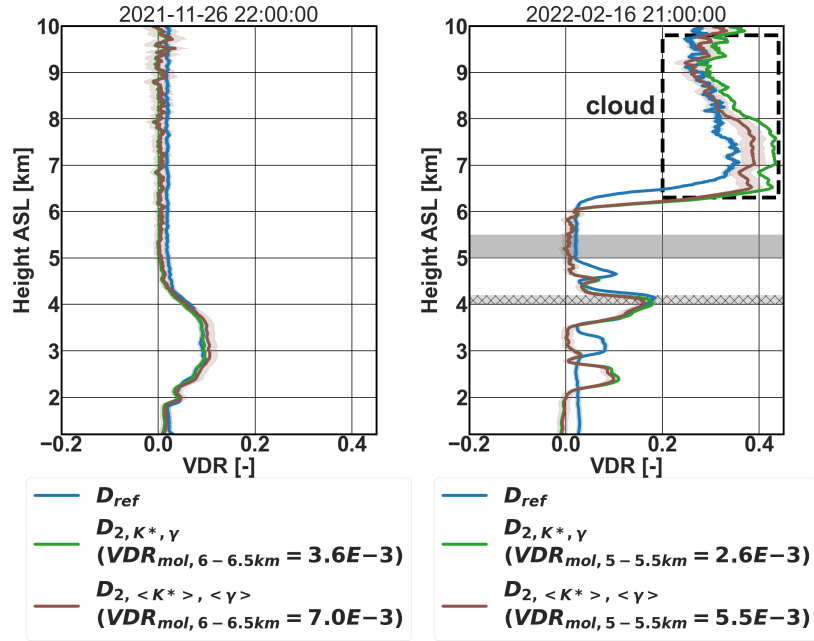
Figure 8. VDR corrected profiles for 26 November 2021 22:00 (left) and 16 February 2022 21:00 (right) using the profile specific (blue) and the average (orange) depolarization parameters for the two periods. Systematic errors of the reference instrument are shown with a blue shade and the statistical uncertainty of the corrected profile D_2 using the average depolarization parameters is shown with a brown shade.

4.2 Three-parameter depolarization characterization

In the previous simplified approach, we neglected the ϵ cross-talk constant. In the three-parameter depolarization characterization, we retrieve all the constants, namely γ, ϵ and K^*. As now there are three unknowns (Eq. 7), determining the cross-talk constant ϵ requires additional input from the measured aerosol column. In addition to the dust and the molecular layer used in the two-parameter approach (δ_{d_1} and δ_{d_m}), we can use a second dust layer or/and a high level ice cloud (δ_{d_2}). The resulting three-parameter equations are:

$$D_{ref_i} = \frac{\delta_{d_i}^* - K^* \gamma}{K^* - \epsilon\, \delta_{d_i}^*} \text{ (i = 1,2)} \tag{14}$$

$$D_m = \frac{\delta_m^* - K^* \gamma}{K^* - \epsilon\, \delta_m^*} \tag{15}$$

This approach introduces an additional constraint to the determination of the parameters. The main reason is that identifying cases with two layers with different depolarization properties measured by both instruments can be rare. As a result of this, reducing the number of selected cases increases the uncertainty of the derived depolarization parameters. Moreover, the two

independent layers can be advected in a different way and therefore it is not necessarily possible to use the same vertical shift correction for both.

During the first period, it was really difficult to identify profiles with two layers above 3 km, mainly because the dust events were remaining at lower altitudes. However, with only a few cases we derived the depolarization parameters seen in Table 2.

270 For the second period, more cases passed the selection criteria mentioned at the beginning of Section 4. Figure 9 shows the time dependence of the resulting parameters for the second period.

Comparing the depolarization parameters from the two approaches (two-parameter vs three-parameter) in Table 2, γ and K^* remained almost unchanged, which satisfies our expectations that the effect of γ dominates the low depolarization layers. This is also confirmed by the values of ϵ which seem to fluctuate close to 0. In Figure 10, the VDR profiles from the two

275 approaches are compared to give a full picture of the vertical deviations. The three-parameter approach generally results in smaller VDR values for the whole profile range. Moreover, the corrected depolarization is noisier for the three-parameter approach. Following these results, we prefer to keep things simple with the two-parameter approach and neglect the effect of ϵ for this instrument.
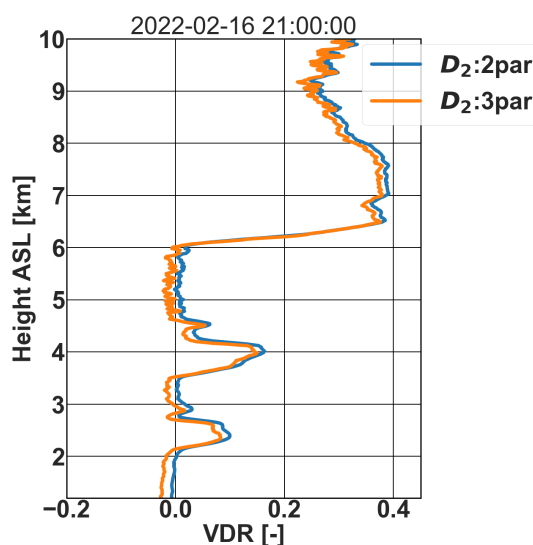
Figure 10. VDR corrected profiles for 16 February 2022 21:00 using the 2-parameter (blue) and the 3-parameter depolarization parameters.

280 ### 4.3 Effective angle of rotation in the depolarisation layout

In (Freudenthaler et al. , 2009) the characterisation of depolarisation is achieved through knowledge of the channel gain ratio, the beamsplitter transmittances and reflectances, and the angle of rotation ϕ between the polarization of the emitter with respect to the frame of reference of the receiver. With the method presented here, instead, the characterisation is achieved through the determination of the parameters K^*, γ, and ϵ. The two representations are equivalent, as shown in Appendix A, and this

285 opens an opportunity to evaluate the angle ϕ from Eq. (A4), using the derived value of γ and assuming that the beamsplitter

(a)

(b)

(c)
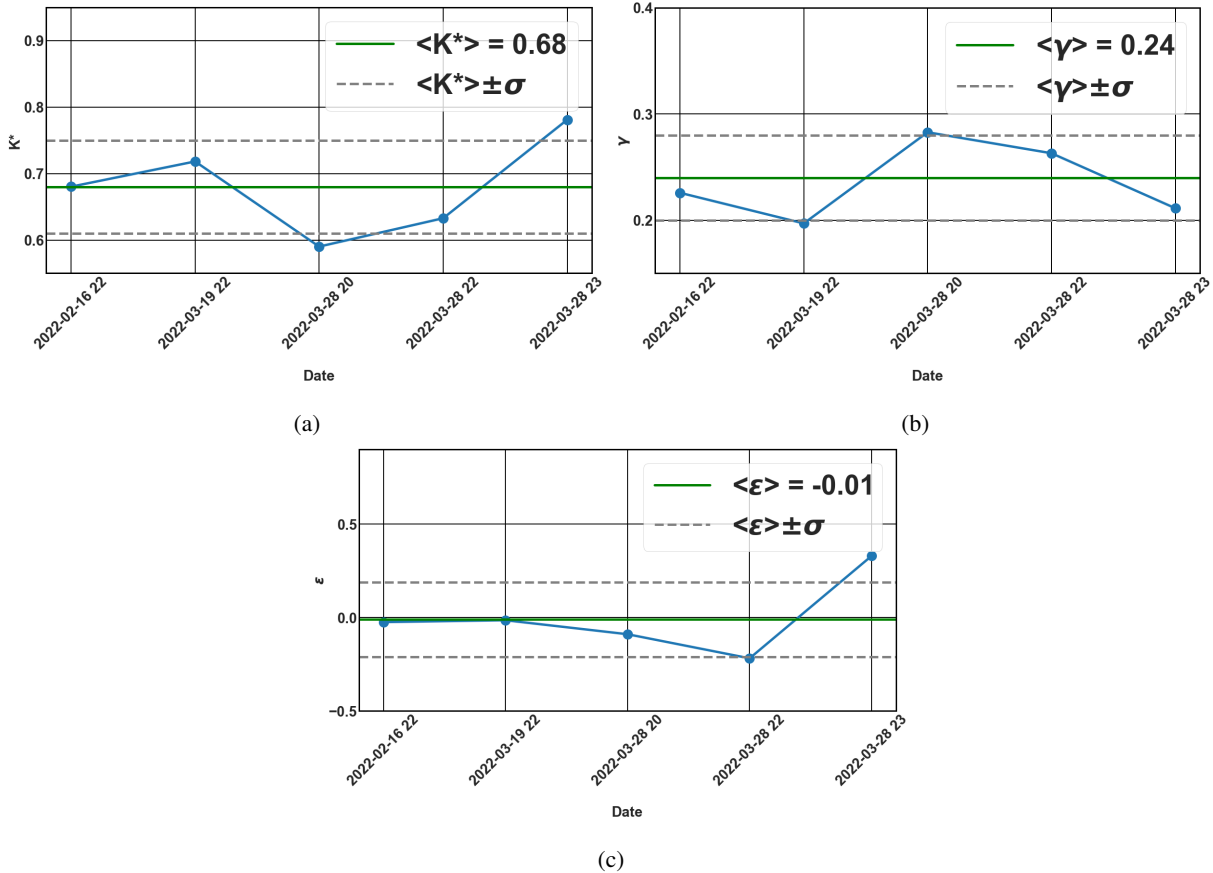
Figure 9. Depolarization parameters vs time for the second period for the three-parameter approach.

parameters $R_p = 1 - T_p$ and $R_s = 1 - T_s$ provided by the manufacturer and given in Table 1 are correct. When doing this exercise, we evaluate that $\phi = (71 \pm 1)°$ and $\phi = (66 \pm 1)°$ for periods 1 and 2, respectively. It is to be noted that the derived angle is not the true angle of rotation, given that in our instrument the angle of rotation is minimized and made to be close to $0°$ by rotation of a HWP in the optical path to maximize the co-polar signal for molecular layers (see Section 3.1). We will therefore call ϕ the effective angle of rotation, being such a useful parameter to characterise the residual cross talk in the system. We recall, moreover, that different beamsplitters were used for both periods and yet the evaluated ϕ of $66 - 71°$ seems not undergoing a huge variation: this may suggest that the issue more likely resides in the emitter (laser depolarisation purity) or an incorrect characterization of the PBS. The value of the effective angle ϕ that we computed is large, indicating that a thorough investigation of both emitting and receiving components of the system is needed.

5 Conclusions

We have presented and demonstrated a method for determining the depolarization parameters using observations from a reference instrument at a nearby location. The presented approach accounts for the cross-talk between the co-polar and cross-polar channels by employing a full set of equations that contain three-parameters, K^*, γ and ϵ, using observations from a reference lidar. We examined the ability of this method to characterize VDR observations from a lidar for which the standard calibration procedures could not fully account for the cross-talk, by utilizing VDR measurements from a reference and previously calibrated lidar. The aim is to obtain the correct depolarization of dust layers and calculations based on (Behrendt and Nakamura , 2002) for the molecular layers.

Results are shown for both a simplified version of this method, the two-parameter approach, where the cross-polar talk into the co-polar channel (ϵ) is neglected and the three-parameter approach where all parameters are to be retrieved. As a whole, the depolarization characterization approach of this paper corrects the depolarization values of both high (i.e. dust) and low depolarizing (i.e. molecular) layers and permits the estimation of the cross-talk parameters. The confidence in the atmospheric depolarization characterization method is confirmed by the reduction of the VDR deviations compared to theoretical VDR molecular values. In the cases examined, for the two-parameter method, the difference between the measured and the theoretical molecular VDR is reduced. In the meantime, at the dust layers VDR the relative difference is reduced up 20% when using the two-parameter instead of the $\pm45°$ calibration.

The application of the three-parameter approach was more challenging, mainly due to the few cases which satisfy the criterion of having two independent aerosol layers above 3 km in one profile. Based on these cases the recalculated parameters K^* and γ did not change more than 4%. We found from the results of the three-parameter approach that ϵ was small enough and therefore could be neglected thus justifying the two-parameter approach.

The calculated depolarization parameters from different cases (11 and 9 timestamps for the first and second periods respectively) vary little over the examined periods, allowing us to apply average parameters calculated for the specific system for VDR correction on longer periods, as it was shown in this study. The application of the average instead of the profile specific depolarization parameters leads to neglectable differences at the high and low depolarized layers, which is acceptable as it remains within the uncertainty of the method. Nevertheless, the system's degradation could affect the depolarization parameters and therefore it is suggested that these are re evaluated on a seasonal basis and at every system upgrade. The applied depolarization parameters are found to reduce significantly the VDR bias in cases where distinct and similar dust layers are observed, thus justifying its retrospective application to be able to use existing valuable data acquired during campaigns.

The EARLINET09 of lidars intercomparison campaign suggests a detailed methodology on the intercomparison approach, requiring all systems to be placed side by side for several days before being deployed at their measuring locations, in order to be able to combine observations from different instruments and techniques (Wandinger , 2016). We need to emphasize that this was not possible in this case, as we are attempting a retrospective characterization of Cyprus 2021 Fall Campaign observations. However, these guidelines should be followed whenever possible, and for the future, we plan an upgrade of the system to have a reliable calibration upfront.

This depolarization characterization method demonstrated for the first time provides a good alternative for systems for which
330   the user doesn't know the values of γ and ϵ a priori and therefore should be applied where traditional calibration procedure
fails to correct the cross-talk in the depolarization channels. According to Bravo-Aranda et al. (2013), lidar systems which are
not well characterized and aligned can lead to large systematic errors in the depolarization values. Reducing the errors related
to the depolarisation observations will therefore reduce the total uncertainty of aerosol typing studies (e.g. Mamouri and Ans-
mann (2014)) or mass concentration retrievals (e.g. Mamali et al. (2018)), for which particle linear depolarization ratio is a
335   key parameter. Using the presented method, valuable data obtained during the Fall Campaign 2021 in Cyprus (manuscript in
preparation Kezoudi et al. (2023)), can be corrected and used for further research on aerosol characteristics and stratification.

Appendix A: How the present treatment of depolarization relates to Freudenthaler et al, 2009

Freudenthaler et al. (2009) treated lidar depolarization extensively and introduced the $\pm 45°$ method for calibration, which is
nowadays of widespread use and a de facto standard. We relate here their equations to the ones developed in the section 2.
340   Whereas in section 2 we don't make any assumptions on the technology employed, the treatment in that paper assumes that
the two polarisation components are separated in the receiver by means of a polarising beamsplitter cube (PBS) of known
characteristics, and that the emitted beam polarisation plane may be rotated with respect to the PBS reference system. We
rewrite here their Eq. (9) for convenience:

$$\delta_F^* = V^* \frac{R_p\left(1 + D\tan^2\phi\right) + R_s\left(\tan^2\phi + D\right)}{T_p\left(1 + D\tan^2\phi\right) + T_s\left(\tan^2\phi + D\right)}, \tag{A1}$$

345   where δ_F^* is the ratio of the two lidar signals, V^* is the channel gain ratio, and ϕ is the angle between the plane of polarization
of the laser and the incidence plane of the PBS. R_p, R_s, T_p, T_s indicate the reflectivities and transmittances of the PBS for
linearly polarised light parallel (p) and perpendicular (s) to the incidence plane, with $R_p \simeq 1 - T_p$, $T_s \simeq 1 - R_s$ ($T_p \ll 1$,
$R_s \ll 1$). The reason why we use the symbols δ_F^* instead of δ^*, and V^* instead of K^*, will be apparent in the following.

This equation has to be compared to our equation (7), which we can rewrite as follows:

350    $$\delta^* = K^* \frac{D + \gamma}{1 + \epsilon D} \tag{A2}$$

The lidar PBS can be basically installed in two logical configurations: with ϕ close to $0°$ or with ϕ close to $90°$. In the first
case, $\delta_F^* = \delta^*$, by comparing Eq. (A1) and (A2) one finds that:

$$K^* = V^* \frac{R_p \tan^2\phi + R_s}{T_p + T_s \tan^2\phi} \tag{A3}$$

Note that in the case that $R_s, T_p \ll 1$ (like in the case of CE376) or $R_p, T_s \ll 1$ (like in the cases of other lidars in the
355   literature) then Eq. A3 can be reduced to $K^* \simeq V^*$.

$$\gamma = \frac{R_p + R_s \tan^2 \phi}{R_p \tan^2 \phi + R_s} \tag{A4}$$

$$\epsilon = \frac{T_p \tan^2 \phi + T_s}{T_p + T_s \tan^2 \phi} \tag{A5}$$

In the case that the system has $\phi = 90°$, then $\delta_F^* = 1/\delta^*$, so that equations equivalent to the above can be derived with a simple derivation (omitted for brevity), and $V^* \simeq 1/K^*$

Appendix B: Vertical shift correction due to spatial separation

A vertical shift appears in the comparison of the profiles of the two instruments mainly due to sloping atmospheric layers between Limassol and Nicosia. This shift can be observed when comparing the most important common dust or cloud layers. A vertical correction is applied on one of the lidar profiles in order to bring the interesting layers tp the same altitudes as the second lidar. An example of this correction is seen in Figure B1, where we consider a vertical correction of $dh = 0.25$ km for the selected timestamp.
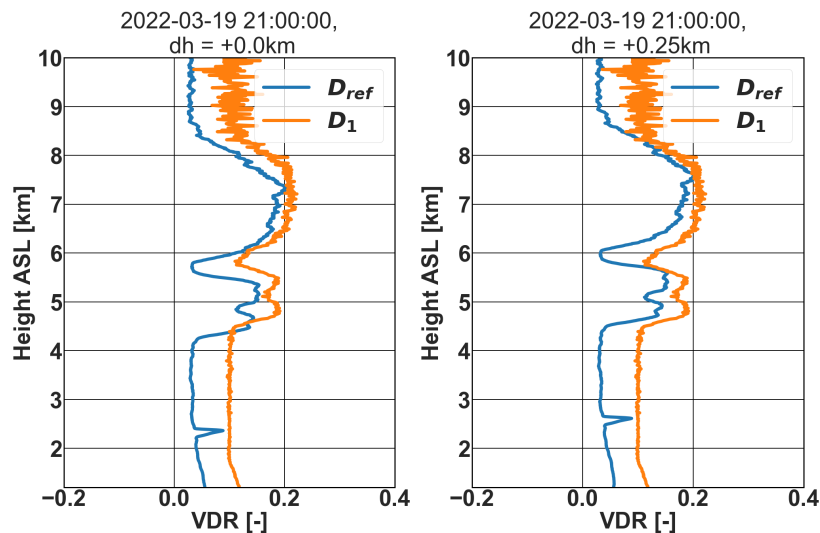
Figure B1. VDR profiles without (left) and with (right) vertical correction.

Appendix C: Uncertainty analysis

The corrected values of D are subject to the propagation of uncertainty. The uncertainty of the two-parameter approach using the average depolarization parameters can be calculated according to GUM (2008) as follows:

$$(\Delta D)^2 = f(\Delta K^{*2}, \Delta\gamma^2, \Delta\delta^{*2}) = \left[\left(\frac{\Delta\delta^*}{\delta^*}\right)^2 + \left(\frac{\Delta K^*}{K^*}\right)^2\right]\left(\frac{\delta^*}{K^*}\right)^2 + (\Delta\gamma)^2 \tag{C1}$$

370

$$= \left[\left(\frac{\Delta P^\perp}{P^\perp}\right)^2 + \left(\frac{\Delta P^\parallel}{P^\parallel}\right)^2 + \left(\frac{\Delta K^*}{K^*}\right)^2\right]\left(\frac{P^\perp}{P^\parallel K^*}\right)^2 + (\Delta\gamma)^2$$

In the above equation, ΔK^* and $\Delta\gamma$ are the standard deviation values presented in Table 2. The measurement uncertainty $\Delta P^\perp$ and $\Delta P^\parallel$ for each polarization channel consists of the uncertainty of the raw counts signal (P_0) and the background correction (B). As the signal is received by a photon counting detector the distribution of the counts follows Poisson statistics and therefore the standard deviation is given by the square root of the number of counts in the measured interval (N).

375
$$\Delta P^{\perp,\parallel} = \sqrt{\left(\Delta P_0^2\right) + \left(\Delta B^2\right)} = \sqrt{N + \frac{\sigma(B)^2}{n}} \tag{C2}$$

where $\sigma(B)$ is the standard deviation of the background correction calculated over n = 67 ranges which corresponds to 1 km.

These calculations are used for deriving the error bars presented in Figure 8.

Appendix D: CE376 optomechanical setup

380 The CE376 consists of two lasers: frequency doubled Nd:YAG emitting at 532nm and a pulsed laser diode for NIR. The backscattered radiation is collected by a Galilean telescope with a diameter of 100mm both in emission and reception. In the detection branch after the telescopes the following can be found: a narrow filter for reducing the background light, a half-wave plate to rotate the plane of polarization and a beam splitter cube to separate the parallel and cross-polarized signals received in the 532nm channel. The signals are recorded by Avalanche Photo Diodes (APDs by SPCM-AQRH modules from Excelitas) at

385 the three reception channels. The APDs are capable of detecting single photon events.
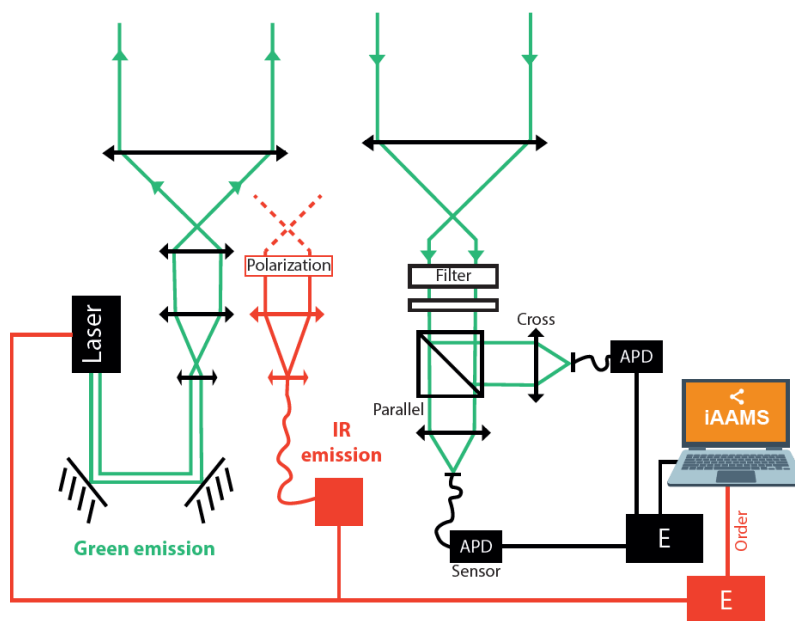
Figure D1. Schematic of the CE376 optomechanical setup.

Author contributions. AP performed the analysis and all the corrections of the data obtained by CIMEL CE376 in Nicosia. AP and FM performed the on site calibration in January and February 2022. EM and AN, operated and analyzed the Polly^{XT} data sharing with AP relevant cases for comparison. AP and FM prepared the initial version of the manuscript. IP revised the manuscript

Competing interests. The authors declare that they have no conflict of interest

390 *Acknowledgements.* The authors would like to thank CIMEL Electronique for their support in the calibration and testing of the CE376 system.

Financial support. This publication has been produced within the framework of the EMME-CARE project which received funding from the European Union's Horizon 2020 Research and Innovation Programme, under grant agreement no. 856612 and from the Cyprus Government.

References

395   Althausen, D., Engelmann, R., Baars, H., Heese, B., Ansmann,A., Müller, D., and Komppula, M.: Portable Raman Lidar Pol-
lyXT for automated profiling of aerosol backscatter, extinction, and depolarization, J. Atmos. Ocean. Tech., 26, 2366–2378,
doi:10.1175/2009JTECHA1304.1, 2009.

Alvarez, J. M., Vaughan, M. A., Hostetler, C. A., Hunt, W. H., Winker, D. M. : Calibration Technique for Polarization-Sensitive Lidars,
Journal of Atmospheric and Oceanic Technology, 23(5), 683-699. Retrieved Dec 2, 2022, https://doi.org/10.1175/JTECH1872.1,2006

400   Ansmann, A., Engelmann, R., Althausen, D., Wandinger, U., Hu, M., Zhang, Y., and He, Q.: High aerosol load over the Pearl River Delta,
China, observed with Raman lidar and Sun photometer, Geophys. Res. Lett., 32, L13815, https://doi.org/10.1029/2005GL023094, 2005.

Ansmann, A., et al.: Ash and fine-mode particle mass profiles from EARLINET-AERONET observations over central Europe after the
eruptions of the Eyjafjallajökull volcano in 2010, J. Geophys. Res., 116, D00U02, https://doi.org/doi:10.1029/2010JD015567, 2011.

Basart, S., Nickovic, S., Terradellas, E., Cuevas, E., García-Pando, C.P., García-Castrillo, G., Werner, E., Benincasa, F. : The
405   WMO SDS-WAS Regional Center for Northern Africa, Middle East and Europe. E3S Web of Conferences. 99. 04008,
https://doi.org/10.1051/e3sconf/20199904008, 2019.

Behrendt, A. and Nakamura T.: Calculation of the calibration constant of polarization lidar and its dependency on atmospheric temperature.
Opt. Express 10, 805-817. https://doi.org/10.1364/OE.10.000805, 2002.

Belegante, L., Bravo-Aranda, J. A., Freudenthaler, V., Nicolae, D., Nemuc, A., Ene, D., Alados-Arboledas, L., Amodeo, A., Pap-
410   palardo, G., D'Amico, G., Amato, F., Engelmann, R., Baars, H., Wandinger, U., Papayannis, A., Kokkalis, P., and Pereira, S. N.:
Experimental techniques for the calibration of lidar depolarization channels in EARLINET, Atmos. Meas. Tech., 11, 1119–1141,
https://doi.org/10.5194/amt-11-1119-2018, 2018.

Bösenberg, J. and Matthias, V.: Earlinet: A european aerosol research lidar network to establish an aerosol climatology. Report. Max-Planck-
Institut fur Meteorologie. 348. 1-191, 2003.

415   Bravo-Aranda, J. A., Navas-Guzman, F., Guerrero-Rascado, J. L., Pérez-Ramírez, D., Granados-Munoz, M. J., and Alados-Arboledas, L.:
Analysis of lidar depolarization calibration procedure and application to the atmospheric aerosol characterization, Int. J. Remote Sens.,
34, 3543–3560, https://doi.org/10.1080/01431161.2012.716546, 2013

Bravo-Aranda, J. A., Belegante, L., Freudenthaler, V., Alados-Arboledas, L., Nicolae, D., Granados-Muñoz, M. J., Guerrero-Rascado, J. L.,
Amodeo, A., D'Amico, G., Engelmann, R., Pappalardo, G., Kokkalis, P., Mamouri, R., Papayannis, A., Navas-Guzmán, F., Olmo, F. J.,
420   Wandinger, U., Amato, F., and Haeffelin, M.: Assessment of lidar depolarization uncertainty by means of a polarimetric lidar simulator,
Atmos. Meas. Tech., 9, 4935–4953, https://doi.org/10.5194/amt-9-4935-2016, 2016.

Brogniez, C., Santer, R., Diallo, B. S., Herman, M., Lenoble, J., and Jäger, H. : Comparative observations of stratospheric aerosols
by ground-based lidar, balloon-borne polarimeter, and satellite solar occultation, J. Geophys. Res., 97(D18), 20805– 20823,
https://doi.org/10.1029/92JD01919 1992.

425   Cairo, F., Di Donfrancesco, G., Adriani, A., Lucio, P. and Federico, F. : Comparison of various linear depolarization parameters mea- sured
by lidar. Appl. Opt. 38, 4425–4432, https://doi.org/10.1364/ao.38.004425, 1999.

Di Girolamo, P., De Rosa, B., Summa, D., Franco, N. and Veselovskii, I.: Measurements of aerosol size and microphysical proper-
ties: A comparison between Raman lidar and airborne sensors. Journal of Geophysical Research: Atmospheres, 127, e2021JD036086.
https://doi.org/10.1029/2021JD036086, 2022.

Di Iorio, T., di Sarra, A., Junkermann, W., Cacciani, M., Fiocco, G., and Fuà, D.: Tropospheric aerosols in the Mediterranean: 1. Microphys-
ical and optical properties, J. Geophys. Res., 108, 4316, https://doi.org/10.1029/2002JD002815, 2003.

Engelmann, R., Kanitz, T., Baars, H., Heese, B., Althausen, D., Fahrwald, A., Wandinger, U., Komppula, M., Stachlewska, I., Amiridis, V.,
Marinou, E., Mattis, I., Linné, H., Ansmann, A.: The automated multiwavelength Raman polarization and water-vapor lidar PollyXT: The
neXT generation. Atmospheric Measurement Techniques. 9. 1767-1784, https://doi.org/10.5194/amt-9-1767-2016, 2016.

Frederick G. Fernald: Analysis of atmospheric lidar observations: some comments, Appl. Opt. 23, 652-653, 1984.

Ferrare, R. A., Melfi, S. H., Whiteman, D. N., Evans, K. D., Poellot, M., and Kaufman, Y. J.: Raman lidar measurements of aerosol extinction
and backscattering: 2. Derivation of aerosol real refractive index, single-scattering albedo, and humidification factor using Raman lidar
and aircraft size distribution measurements, J. Geophys. Res., 103(D16), 19673– 19689, https://doi.org/10.1029/98JD01647, 1998.

Fowler, L. D., and Randall, D. A.: Interactions between cloud microphysics and cumulus convection in a general circulation model. Journal
of the Atmospheric Sciences, 59(21), 3074–3098, https://doi.org/10.1175/1520-0469(2002)059<3074:IBCMAC>2.0.CO;2, 2002.

Freudenthaler, V., Esselborn, M., Wiegner, M., Heese, B., Tesche, M., Ansmann, A., Muller, D., Althausen, D., Wirth, M., Fix, A., Ehret,
G., Knippertz, P., Toledano, C., Gasteiger, J., Garhammer, M., and Seefeldner, M.: Depolarization ratio profiling at several wavelengths in
pure Saharan dust during SAMUM 2006, Tellus B, 61, 165–179, doi:10.1111/j.1600-0889.2008.00396.x, 2009.

Freudenthaler, V.: About the effects of polarising optics on lidar signals and the Δ90-calibration. Atmospheric Measurement Techniques
Discussions. 1-82. doi: 10.5194/amt-2015-338 2016.

Groß, S., Tesche, M., Freudenthaler, V., Toledano, C., Wiegner, M., Ansmann, A., Althausen, D., and Seefeldner, M.: Characterization of
Saharan dust, marine aerosols and mixtures of biomass burning aerosols and dust by means of multi-wavelength depolarization- and
Raman-measurements during SAMUM-2, Tellus B, 63, 706–724, doi:10.1111/j.1600-0889.2011.00556.x, 2011.

Hoffmann, A., Ritter, C., Stock, M., Maturilli, M., Eckhardt, S., Herber, A., and Neuber, R.: Lidar measurements of the Kasatochi aerosol
plume in August and September 2008 in Ny-Ålesund, Spitsbergen. Journal of Geophysical Research Atmospheres, 115(19), 1–12,
https://doi.org/10.1029/2009JD013039, 2010.

IPCC, 2021: Climate Change 2021: The Physical Science Basis. Contribution of Working Group I to the Sixth Assessment Report
of the Intergovernmental Panel on Climate Change [Masson-Delmotte, V., P. Zhai, A. Pirani, S.L. Connors, C. Péan, S. Berger, N.
Caud, Y. Chen, L. Goldfarb, M.I. Gomis, M. Huang, K. Leitzell, E. Lonnoy, J.B.R. Matthews, T.K. Maycock, T. Waterfield, O.
Yelekçi, R. Yu, and B. Zhou (eds.)]. Cambridge University Press, Cambridge, United Kingdom and New York, NY, USA, 2391 pp.,
https://doi.org/10.1017/9781009157896, 2021.

JCGM 100:2008 Evaluation of Measurement Data—Guide to the Expression of Uncertainty in Measurement.

Kezoudi, M., Keleshis, C., Antoniou, P., Biskos, G., Bronz, M., Constantinides, C., Desservettaz, M., Gao, R.-S., Girdwood, J., Harnetiaux,
J., Kandler, K., Leonidou, A., Liu, Y., Lelieveld, J., Marenco, F., Mihalopoulos, N., Močnik, G., Neitola, K., Paris, J.-D., Pikridas, M.,
Sarda-Esteve, R., Stopford, C., Unga, F., Vrekoussis, M., Sciare, J.: The Unmanned Systems Research Laboratory (USRL): A New Facility
for UAV-Based Atmospheric Observations. Atmosphere 2021, 12, 1042, https://doi.org/10.3390/atmos12081042, 2021.

Kiriakidis, P., Gkikas, A., Papangelis, G., Kushta, J., Christoudias, T., Drakaki, E., Proestakis, E., Marinou, E., Gialitaki, A., Kampouri, A.,
Spyrou, C., Benedetti, A., Rennie, M., Straume, A. G., Retscher, C., Dandocsi, A., Sciare, J., and Amiridis, V.: The impact of assimilating
AEOLUS wind data on regional Aeolian dust model simulations using WRF-Chem. , EGU General Assembly 2022, Vienna, Austria,
23–27 May 2022, EGU22-980, https://doi.org/10.5194/egusphere-egu22-980, 2022.

James D. Klett: Lidar inversion with variable backscatter/extinction ratios. Appl. Opt. 24, 1638-1643, 1985

Krueger, D. A., Caldwell, L. M., She, C. Y., and Alvarez , R. J., II.: Self-consistent Method for Determining Vertical Profiles of Aerosol and Atmospheric Properties Using a High Spectral Resolution Rayleigh-Mie Lidar, Journal of Atmospheric and Oceanic Technology, 10(4), 533-545, https://doi.org/10.1175/1520-0426(1993)010<0533:SCMFDV>2.0.CO;2, 1993.

470 Mamali, D., Marinou, E., Sciare, J., Pikridas, M., Kokkalis, P., Kottas, M., Binietoglou, I., Tsekeri, A., Keleshis, C., Engelmann, R., Baars, H., Ansmann, A., Amiridis, V., Russchenberg, H., and Biskos, G.: Vertical profiles of aerosol mass concentration derived by unmanned airborne in situ and remote sensing instruments during dust events, Atmos. Meas. Tech., 11, 2897–2910, https://doi.org/10.5194/amt-11-2897-2018, 2018.

Mamouri, R. E. and Ansmann, A.: Fine and coarse dust separation with polarization lidar, Atmos. Meas. Tech., 7, 3717–3735,
475 https://doi.org/10.5194/amt-7-3717-2014, 2014.

Marenco, F., and R. J. Hogan: Determining the contribution of volcanic ash and boundary layer aerosol in backscatter lidar returns: A three-component atmosphere approach, J. Geophys. Res., 116, D00U06, https://doi.org/10.1029/2010JD015415, 2011.

Osborne, M. J., de Leeuw, J., Witham, C., Schmidt, A., Beckett, F., Kristiansen, N., Buxmann, J., Saint, C., Welton, E. J., Fochesatto, J., Gomes, A. R., Bundke, U., Petzold, A., Marenco, F., and Haywood, J.: The 2019 Raikoke volcanic eruption – Part 2: Particle-phase
480 dispersion and concurrent wildfire smoke emissions, Atmos. Chem. Phys., 22, 2975–2997, https://doi.org/10.5194/acp-22-2975-2022, 2022.

Osborne, M. J., de Leeuw, J., Witham, C., Schmidt, A., Beckett, F., Kristiansen, N., Buxmann, J., Saint, C., Welton, E. J., Fochesatto, J., Gomes, A. R., Bundke, U., Petzold, A., Marenco, F., and Haywood, J.: Developing Resilience to Icelandic Volcanic Eruptions, , PhD thesis, University of Exeter, Exeter, http://hdl.handle.net/10871/129640, 2022.

485 Paschou, P., Siomos, N., Tsekeri, A., Louridas, A., Georgoussis, G., Freudenthaler, V., Binietoglou, I., Tsaknakis, G., Tavernarakis, A., Evangelatos, C., von Bismarck, J., Kanitz, T., Meleti, C., Marinou, E., and Amiridis, V.: The eVe reference polarisation lidar system for the calibration and validation of the Aeolus L2A product, Atmos. Meas. Tech., 15, 2299–2323, https://doi.org/10.5194/amt-15-2299-2022, 2022

Reagan, J. A., Spinhirne, J. D., Byrne, D. M., Thomson, D. W., Pena, R. G. D., and Mamane, Y. : Atmospheric Particulate Properties Inferred
490 from Lidar and Solar Radiometer Observations Compared with Simultaneous In Situ Aircraft Measurements: A Case Study, Journal of Applied Meteorology and Climatology, 16(9), 911-928, https://doi.org/10.1175/1520-0450(1977)016<0911:APPIFL>2.0.CO;2, 1977.

Sassen, K., Zhu, J., Webley, P., Dean, K. and Cobb, P.: Volcanic ash plume identification using polarization lidar: Augustine eruption, Alaska. Geophysical research letters. 34. L08803, https://doi.org/10.1029/2006GL027237, 2007.

Senior, C. A., and J. F. B. Mitchell:Carbon Dioxide and Climate. The Impact of Cloud Parameterization, Journal of Climate 6, 3 (1993):
495 393-418, accessed Sep 2, 2022, https://doi.org/10.1175/1520-0442(1993)006<0393:CDACTI>2.0.CO;2, 1993.

Tesche, M., Ansmann, A., Müller, D., Althausen, D., Engelmann, R., Freudenthaler, V., and Groß, S.: Vertically resolved separation of dust and smoke over Cape Verde using multiwavelength Raman and polarization lidars during Saharan Mineral Dust Experiment 2008, J. Geophys. Res., 114, D13202, https://doi.org/10.1029/2009JD011862, 2009.

Tesche, M., Groß, S., Ansmann, A., Müller, D., Althausen, D., Freudenthaler, V., and Esselborn, M.: Profiling of Saharan dust and
500 biomass-burning smoke with multiwavelength polarization Raman lidar at Cape Verde, Tellus B, 63, 649–676, doi:10.1111/j.1600-0889.2011.00548.x, 2011.

Toon, O. B., Tabazadeh, A., Browell, E. V., and Jordan, J.: Analysis of lidar observations of Arctic polar stratospheric clouds during January 1989, J. Geophys. Res., 105(D16), 20589– 20615, https://doi.org/10.1029/2000JD900144, 2000.

Van de Hulst, H.C.: Light Scattering by Small Particles. John Wiley and Sons, New York; Chapman and Hall, London, https://doi.org/10.1063/1.3060205, 1957.

Wandinger, U., Freudenthaler, V., Baars, H., Amodeo, A., Engelmann, R., Mattis, I., Groß, S., Pappalardo, G., Giunta, A., D'Amico, G., Chaikovsky, A., Osipenko, F., Slesar, A., Nicolae, D., Belegante, L., Talianu, C., Serikov, I., Linné, H., Jansen, F., Apituley, A., Wilson, K. M., de Graaf, M., Trickl, T., Giehl, H., Adam, M., Comerón, A., Muñoz-Porcar, C., Rocadenbosch, F., Sicard, M., Tomás, S., Lange, D., Kumar, D., Pujadas, M., Molero, F., Fernández, A. J., Alados-Arboledas, L., Bravo-Aranda, J. A., Navas-Guzmán, F., Guerrero-Rascado, J. L., Granados-Muñoz, M. J., Preißler, J., Wagner, F., Gausa, M., Grigorov, I., Stoyanov, D., Iarlori, M., Rizi, V., Spinelli, N., Boselli, A., Wang, X., Lo Feudo, T., Perrone, M. R., De Tomasi, F., and Burlizzi, P.: EARLINET instrument intercomparison campaigns: overview on strategy and results, Atmos. Meas. Tech., 9, 1001–1023, https://doi.org/10.5194/amt-9-1001-2016, 2016.